

UC Berkeley

UC Berkeley Previously Published Works

Title

Runaway Carbon Dioxide Conversion Leads to Enhanced Uptake in a Nanohybrid Form of Porous Magnesium Borohydride.

Permalink

<https://escholarship.org/uc/item/4fs0k8mg>

Journal

Advanced materials (Deerfield Beach, Fla.), 31(44)

ISSN

0935-9648

Authors

Jeong, Sohee
Milner, Phillip J
Wan, Liwen F
et al.

Publication Date

2019-11-01

DOI

10.1002/adma.201904252

Peer reviewed

Runaway Carbon Dioxide Conversion Leads to Enhanced Uptake in a Nanohybrid Form of Porous Magnesium Borohydride

Sohee Jeong, Phillip J. Milner, Liwen F. Wan, Yi-Sheng Liu, Julia Oktawiec, Edmond W. Zaia, Alexander C. Forse, Noemi Leick, Thomas Gennett, Jinghua Guo, David Prendergast,* Jeffrey R. Long,* and Jeffrey J. Urban*

ABSTRACT: Leveraging molecular-level controls to enhance CO₂ capture in solid-state materials has received tremendous attention in recent years. Here, a new class of hybrid nanomaterials constructed from intrinsically porous γ -Mg(BH₄)₂ nanocrystals and reduced graphene oxide (MBHg) is described. These nanomaterials exhibit kinetically controlled, irreversible CO₂ uptake profiles with high uptake capacities (>19.9 mmol g⁻¹) at low partial pressures and temperatures between 40 and 100 °C. Systematic experiments and first-principles calculations reveal the mechanism of reaction between CO₂ and MBHg and unveil the role of chemically activated, metastable (BH₃-HCOO)⁻ centers that display more thermodynamically favorable reaction and potentially faster reaction kinetics than the parent BH₄⁻ centers. Overall, it is demonstrated that size reduction to the nanoscale regime and the generation of reactive, metastable intermediates improve the CO₂ uptake properties in metal borohydride nanomaterials.

fossil fuels will necessarily continue in the near term, carbon capture (and sequestration) is widely acknowledged as a necessary carbon abatement strategy. As such, scientific research in recent years has focused with new energy on developing fundamental understanding and control of CO₂ uptake in solid-state materials.^[1-7] In particular, the molecular level control of CO₂ adsorption/absorption in porous structures with a high density of strong binding sites has been targeted as a means of tailoring their performance for various carbon capture processes. For example, porous carbons, zeolite, and metal-organic frameworks (MOFs) have been modified with various N-functionalities to enhance their reactivity toward CO₂.^[5-8] Tunable porous solids are capable of achieving both high capacities and high selectivities for binding CO₂,^[4-10] rendering them potential candidates for post-combustion CO₂ capture at low pressures (<0.15 bar) and mild temperatures (25–70 °C).^[2,3,8,11] Aside from postcombustion

Anthropogenic carbon dioxide (CO₂) emissions, largely derived from the burning of fossil fuels, are among the largest contributors to global warming. Given that global dependence on

binding CO₂,^[4-10] rendering them potential candidates for post-combustion CO₂ capture at low pressures (<0.15 bar) and mild temperatures (25–70 °C).^[2,3,8,11] Aside from postcombustion

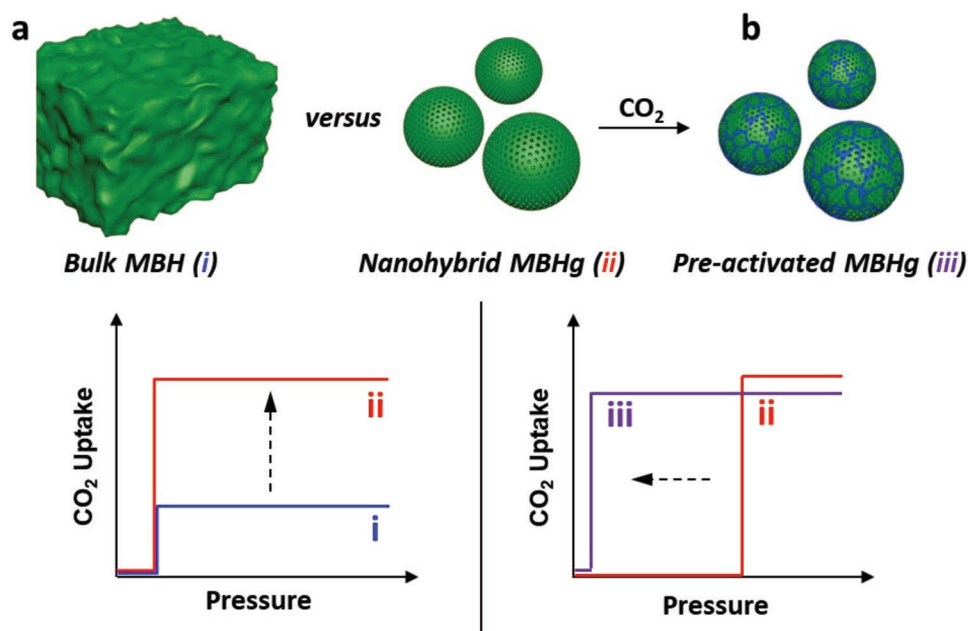
Dr. S. Jeong, Dr. L. F. Wan, Dr. E. W. Zaia, Dr. D. Prendergast, Dr. J. J. Urban
The Molecular Foundry
Lawrence Berkeley National Laboratory
Berkeley, CA 94720, USA
E-mail: DGPrendergast@lbl.gov; jjurban@lbl.gov
Prof. P. J. Milner, J. Oktawiec, Prof. A. C. Forse, Prof. J. R. Long
Department of Chemistry
University of California
Berkeley, CA 94720, USA
E-mail: jrlong@berkeley.edu
Prof. P. J. Milner, J. Oktawiec, Prof. J. R. Long
Materials Sciences Division
Lawrence Berkeley National Laboratory
Berkeley, CA 94720, USA
Prof. P. J. Milner
Department of Chemistry and Chemical Biology
Cornell University
Ithaca, NY 14853, USA

Dr. L. F. Wan
Lawrence Livermore National Laboratory
Livermore, CA 94550, USA
Dr. Y.-S. Liu, Dr. J. Guo
The Advanced Light Source
Lawrence Berkeley National Laboratory
Berkeley, CA 94720, USA
Dr. N. Leick, Dr. T. Gennett
National Renewable Energy Laboratory Colorado
Colorado, CO 80401, USA
Dr. T. Gennett
Chemistry Department
Colorado School of Mines
1012 14th Street, Golden, CO 80401, USA
Dr. J. Guo
Department of Chemistry and Biochemistry
University of California
Santa Cruz, CA 95064, USA
Prof. J. R. Long
Department of Chemical and Biomolecular Engineering
University of California
Berkeley, CA 94720, USA

CO₂ capture, there is also great interest in materials that can reduce CO₂ concentrations for life support in confined spaces such as in spacecrafts, submarines, or scuba suits.^[12,13] These applications motivated extensive research into porous solids as potential lightweight, more efficient replacements for existing solution-phase scrubbers such as aqueous alkanolamines, or common nonporous CO₂ scrubbers such as CaO.^[9,11] Herein, we demonstrate that hybrid nanomaterials constructed by reducing the size of intrinsically porous γ -Mg(BH₄)₂ (MBH) crystals to the nanoscale regime within reduced graphene oxide (rGO) exhibit increased CO₂ uptake compared to the parent bulk materials. Extensive molecular-level characterization of the CO₂ reaction mechanism in this material reveals that its abrupt CO₂ uptake profiles result from a slow initial reaction with CO₂ followed by a faster reaction that is computationally predicted to be highly exothermic. In addition, by systematically studying the kinetics of CO₂ reaction with these γ -Mg(BH₄)₂/rGO nanomaterials (MBHg), we prepared metastable, “activated” versions of the open-framework borohydrides that display improved CO₂ reaction kinetics as well as improved uptake at lower CO₂ pressures (e.g., <0.1 bar) (Scheme 1).

MBH has recently emerged as a potentially promising material for CO₂ capture applications due to its naturally porous structure (33% void volume), high theoretical internal surface area (1160 m² g⁻¹),^[14,15] and high CO₂ uptake (theoretical maximum CO₂ uptake of 37.0 mol kg⁻¹ assuming a 1:1 reaction between CO₂ and each BH₄⁻ unit). However, in practice, bulk MBH operates far from these limits; recent reports have shown that this material exhibits a maximum CO₂ uptake of only 12 mol kg⁻¹ under 1 bar of CO₂ at 30 °C.^[11] Additionally, MBH and other metal borohydrides such as LiBH₄ and NaBH₄ react very slowly with CO₂ in the solid state, often

necessitating high temperatures or solvent to achieve reasonable reaction rates.^[16,17] In order to increase the accessibility of CO₂ reaction sites and potentially improve the reaction kinetics, we first synthesized MBH nanomaterials by modifying the previously reported syntheses^[18,19] to reduce the size of MBH to the nanoscale regime, as described in detail in Methods (Supporting Information). In our synthetic process, we employed rGO as a supporting matrix for nanoscale MBH, affording the nanohybrid MBHg.^[19] The amount of rGO in the material is 3.0 wt% overall. The resulting material was characterized by transmission electron microscopy (TEM), scanning transmission electron microscopy (STEM), and powder X-ray diffraction (PXRD) (Figure 1a–c, Figure S1, Supporting Information). Elemental analysis confirmed that as-synthesized MBHg is composed of Mg, B, and C and provided further evidence for the nanosized dimensions of the material (Figure S2, Supporting Information). The MBH nanoparticles were found to be less than 50 nm in diameter based on the TEM images. In addition, Scherrer analysis of the PXRD patterns indicated an average crystallite size of \approx 28 nm (Table S1, Supporting Information). The crystallite size of MBH without rGO is several micrometers, indicating that the rGO indeed serves as a suitable supporting matrix for the MBH nanoparticles (Figure S3, Supporting Information). Notably, the Brunauer–Emmett–Teller (BET) N₂ specific surface area of MBHg at 77 K is 640 m² g⁻¹ (Figure S4, Supporting Information), which is nearly double that of a previous report of the bulk material (325 m² g⁻¹)^[15] as well as bulk MBH prepared in this work (348 m² g⁻¹, Figure S3, Supporting Information). The nanocomposites have porosity with a predicted specific pore volume of \approx 0.4 cm³ g⁻¹ (Figure S4, Supporting Information), which is in good agreement with naturally porous bulk MBH.



Scheme 1. a) Relative to bulk γ -Mg(BH₄)₂ (MBH), the nanohybrid MBHg prepared in this work—consisting of nanoscale MBH on reduced graphene oxide (rGO)—exhibits greater CO₂ uptake (i and ii) as a result of an increase in accessible reaction sites. b) Pre-activating MBHg with flowing CO₂ leads to further enhancement of low-pressure CO₂ uptake (iii). The blue, red, and purple lines represent the CO₂ uptake profiles for bulk MBH, MBHg, and pre-activated MBHg, respectively.

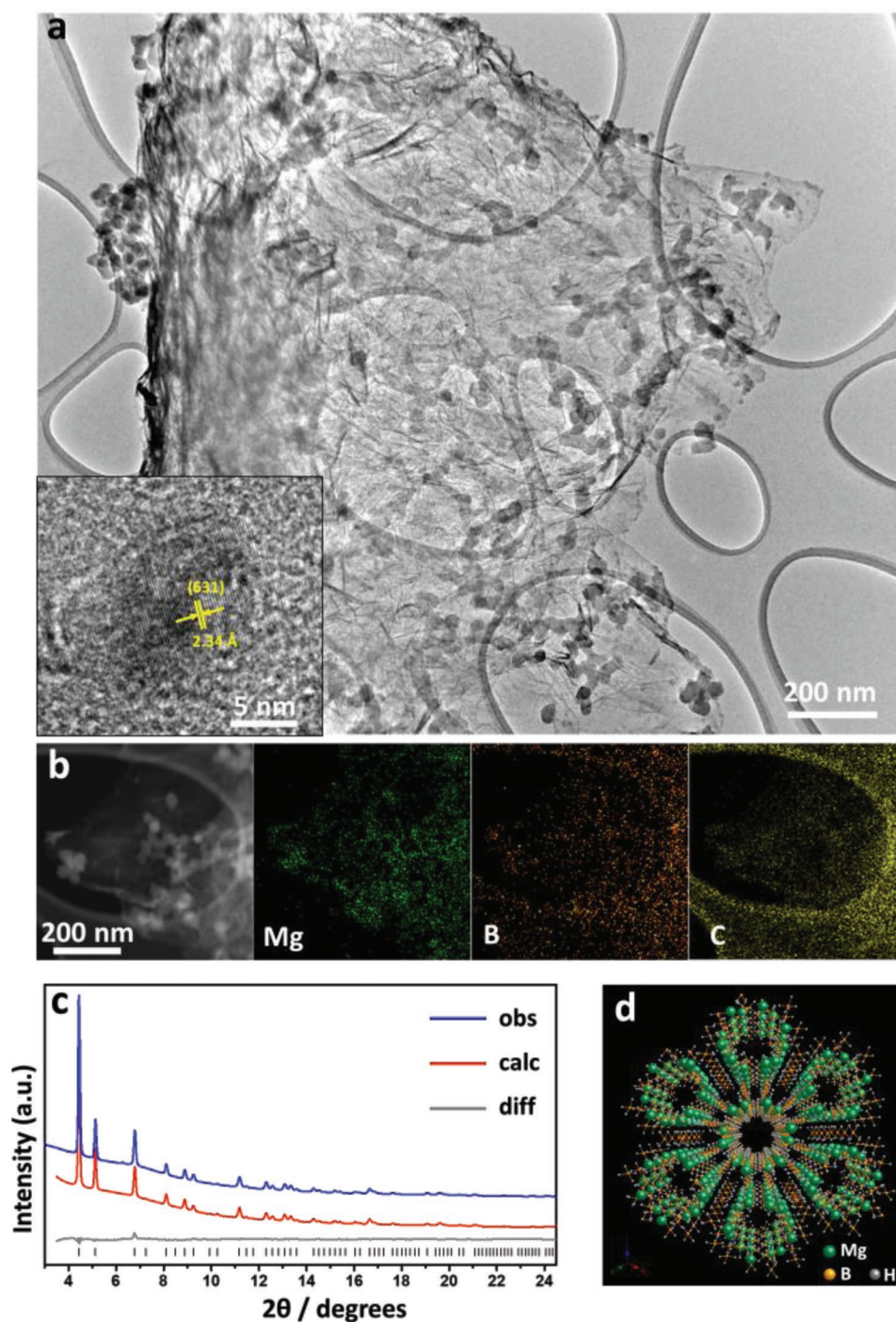


Figure 1. a) TEM images of MBHg. The inset shows the corresponding HRTEM images of MBHg. b) STEM image and the corresponding energy-dispersive X-ray spectroscopy (EDS) mapping of MBHg for Mg, B, and C, respectively. c) PXRD and Rietveld refinement of MBHg at 298 K. The blue and red lines represent the observed and calculated diffraction patterns, respectively. The gray line represents the difference between observed and calculated patterns, and the black tick marks indicate calculated Bragg peak positions. d) Structural model of γ -Mg(BH₄)₂ illustrating its porous structure. The green, orange, and gray spheres represent Mg, B, and H atoms, respectively.

In addition, Rietveld analysis using PXRD patterns of MBHg confirms that the as-synthesized material contains γ -Mg(BH₄)₂ (Figure 1c,d).

The volumetric CO₂ uptake profiles for MBHg at various temperatures are shown in Figure 2. The material exhibited

very high 1 bar CO₂ uptake of 17.9, 19.9, 25.5, and 23.2 mmol g⁻¹ in total mass at 25, 40, 70, and 100 °C, respectively—as much as a 260% improvement in CO₂ uptake over the previous best in class for metal borohydrides (Figure 2a). Even at 0.15 bar, high uptakes of ≈18, 23, and 18 mmol g⁻¹ were

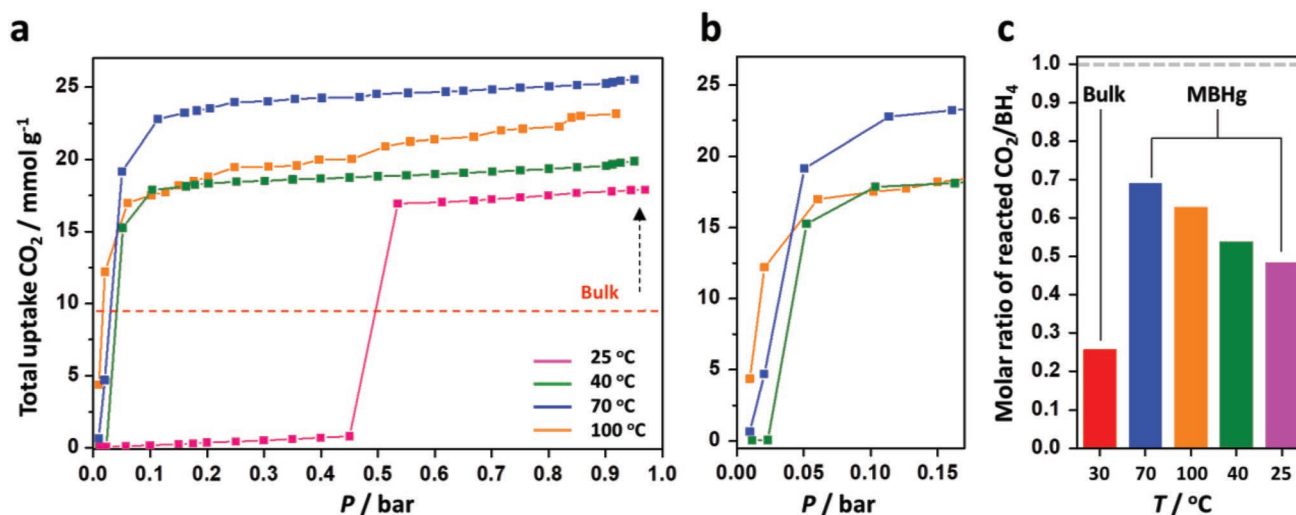


Figure 2. a) 25, 40, 70, and 100 °C equilibrium CO₂ uptake profiles of MBHg. A data point was considered equilibrated after <0.01% volume change occurred during a 10 s equilibration interval. The red dashed line indicates the uptake of CO₂ at 1 bar in bulk MBH at 30 °C.^[15] b) Expanded view of the data in (a) for CO₂ uptake at 40, 70, and 100 °C and pressures ranging from 0 to 0.17 bar. c) Molar ratio of reacted CO₂/BH₄⁻ of bulk MBH and MBHg. The gray dashed line indicates a 1:1 reaction between CO₂ and each BH₄⁻ unit corresponding to the theoretical uptake of 37.0 mol CO₂ kg⁻¹.

reached at 40, 70, and 100 °C, respectively (Figure 2b). The CO₂ uptake at 1 bar and 70 °C (25.5 mmol g⁻¹) corresponds to reaction at ≈68% of available reaction sites (1:1.45 reaction between CO₂ and BH₄⁻) (Figure 2c). Notably, the nanostructured MBHg shows significantly higher capacities compared to previous reports of bulk MBH, which demonstrated CO₂ uptake capacities of ≈9.5 mmol g⁻¹ at 30 °C and 1 bar (≈10.5 mmol g⁻¹ at 25 °C for the bulk MBH prepared in this work, see Figure S3, Supporting Information), corresponding to reaction at ≈25% of available reaction sites (a 1:3.89 reaction between CO₂ and BH₄⁻).^[15] Unlike MBHg, the peaks for the low-index planes of bulk MBH still remained with longer exposure times (2.0 d at 1 bar and 25 °C) (Figure S5, Supporting Information). The CO₂ uptake of nanostructured MBHg is also higher than the best performing oxide material CsO₂/CaO (≈15 mmol g⁻¹ at 600 °C and 0.29 bar).^[20,21] The nanoscale size of the MBHg reduces molecular diffusion lengths and leads to a higher surface area than the bulk material, which leads to improved reactivity of this material toward CO₂. However, the uptake in MBHg is irreversible, as demonstrated by the temperature programmed desorption-mass spectrometry analysis of fully CO₂-saturated MBHg in the temperature range from 25 to 750 °C (Figure S6, Supporting Information). Upon heating, the samples decompose to evaluate not only CO₂ but also other species including the intermediates in the reaction of MBHg with CO₂ that we predict (see next).

The CO₂ uptake profile of MBHg features an abrupt increase at 25 °C (Figure 2a). While minimal uptake occurs at pressures below ≈0.45 bar, above this pressure MBHg takes up more than 15 mmol g⁻¹ of CO₂. Notably, when the sample was allowed to equilibrate for longer periods of time, initial CO₂ uptake at 25 °C occurred at lower pressures (Figure S7, Supporting Information). These results indicate that CO₂ uptake is not at thermodynamic equilibrium under these conditions, and the uptake profiles in Figure 2 instead are influenced by kinetic effects, such as limited reaction or diffusion of CO₂ within the

material. Therefore, the distinct “jump” in the uptake profiles likely results from the sudden favorable reaction with CO₂—at a threshold pressure and temperature—following slow initial activation of MBHg by CO₂. Indeed, supporting this rationale, at 25 °C, the reaction is slower and relatively high pressures of CO₂ are needed for uptake to occur, while at higher temperatures, substantial CO₂ uptake in MBHg occurs <0.17 bar (Figure 2b, vide infra).

To further understand the mechanism of CO₂ uptake in MBHg, we studied the reaction process by PXRD as well as Fourier-transform infrared (FTIR), Raman, X-ray absorption (XAS) spectroscopies, ¹³C solid-state nuclear magnetic resonance (SSNMR), TEM, STEM, and energy-dispersive X-ray spectroscopy (EDS). (Figure 3 and Figures S8–S11, Supporting Information). In order to produce metastable CO₂-reacted phases of MBHg for further study, as-synthesized MBHg was exposed to 0.5 bar of CO₂ at room temperature for 1 h (MBHg-1h) and 2 h (MBHg-2h). Morphological and elemental analysis confirmed that MBHg-1h and MBHg-2h have similar morphologies compared to MBHg and are composed of Mg, B, and C (Figures S8 and S9, Supporting Information). In addition, fully CO₂-saturated MBHg samples (MBHg-sat) were obtained after CO₂ uptake experiments of MBHg at 25 °C. Refinement analysis of PXRD patterns of all MBHg samples showed minimal changes in the unit cell parameters, bond lengths, and density upon reaction with CO₂ (Table S2, Supporting Information). However, the increasingly CO₂-loaded MBHg samples displayed lower intensity peaks, with the peaks for the high-index planes indistinguishable in MBHg-2h (Figures S10 and S11, Supporting Information). Thus, as MBHg reacts with CO₂ it becomes increasingly amorphous and loses porosity, which is also supported by the decreased BET surface area (16.5 m² g⁻¹) and pore volume (0.06 cm³ g⁻¹) of MBHg-sat compared to MBHg. With longer exposure times (2 d at 1 bar and 25 °C), all of the diffraction peaks disappeared and the materials became completely amorphous (Figure S5, Supporting Information).

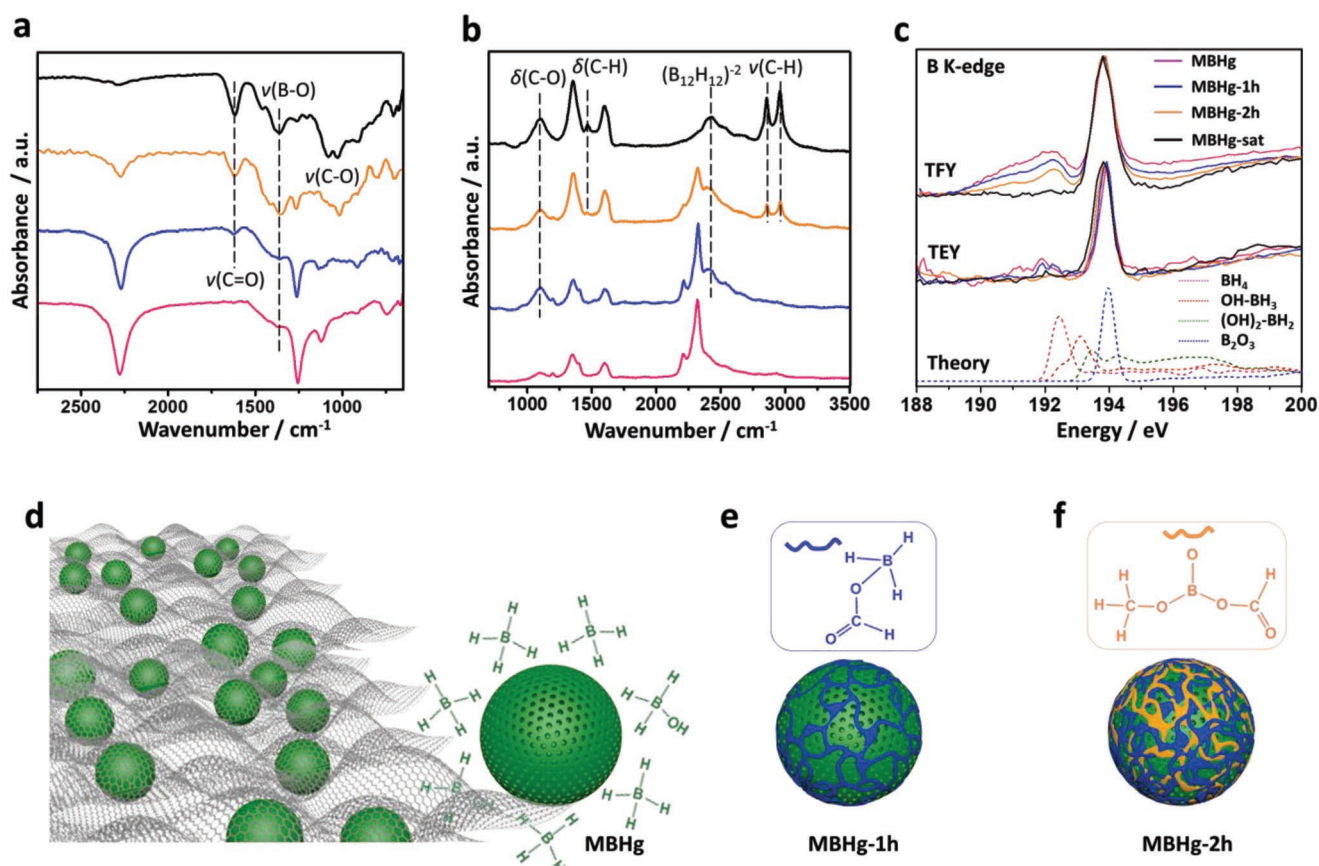


Figure 3. Experimental characterization and simulation of the CO_2 reaction products in MBHg. a) FTIR, b) Raman spectra, and c) B K-edge XAS spectra of as-synthesized MBHg (pink), MBHg exposed to 0.5 bar CO_2 at room temperature for 1 h (MBHg-1h, blue) or 2 h (MBHg-2h, orange) and fully saturated MBHg (MBHg-sat, black). With increasing CO_2 exposure time, the signal at ≈ 192 eV in the B K-edge XAS, corresponding to a hydride, decreases. Upon complete saturation, this feature disappears completely as shown in the TFY measurement. B K-edge spectra were normalized to standard boron oxide (B_2O_3) to facilitate peak analysis. d–f) Schematic illustration of unactivated MBHg, MBHg-1h, and MBHg-2h, respectively.

FTIR, Raman spectroscopy, and ^{13}C SSNMR were used to identify the products of the reaction between MBHg and CO_2 (Figure 3a,b). For MBHg at room temperature (pink data), the Raman spectrum of rGO shows two major features, the G band at 1575 cm^{-1} and the D band at 1350 cm^{-1} .^[22] In the IR spectrum, BH_4^- bands appear at 1117 , 1259 , and 2300 cm^{-1} .^[23] Upon exposure to CO_2 , the IR spectrum of the MBHg-1h sample (blue curve, Figure 3a) features a weak $\nu(\text{C}=\text{O})$ mode at 1618 cm^{-1} , which increases in intensity with longer CO_2 exposure times (yellow and black curves); the intensity of all absorption bands for BH_4^- correspondingly decrease. In the Raman spectra, two distinct peaks gradually grow in at 1101 and 2423 cm^{-1} , corresponding to $\text{C}-\text{O}$ ^[24] and $(\text{B}_{12}\text{H}_{12})^{2-}$ anion (the well-known by-product of dehydrogenated BH_4^- ^[25]) stretching peaks, respectively. Together, these results indicate that a chemical reaction between BH_4^- and CO_2 results in the formation of BH_3 and HCOO^- (see Figure 3e), in which CO_2 is reduced by nucleophilic addition of H^- . Notably, formate is a well-known intermediate in the CO_2 reduction process upon reaction of CO_2 with borohydride.^[26,27] For MBHg-1h and MBHg-2h, $\nu(\text{CH}_3)$ peaks for methoxide are clearly observed at 1474 , 2855 , and 2961 cm^{-1} .^[24] Methoxide formation likely arises due to further reduction of the initially formed formate centers

($\text{BH}_3-\text{HCOO}^-$) (Figure 3f). As the reaction time increases, the C–H and C=O stretches increase in intensity due to the progressive generation of both formate and methoxide. After MBHg fully reacts with CO_2 , the BH_4^- modes become almost nonexistent.^[28]

Additionally, the product of the reaction between MBHg and CO_2 was analyzed by SSNMR spectroscopy. The sample was prepared by exposing MBHg to ≈ 0.5 bar of ^{13}C -labeled CO_2 at room temperature for 2 h. The ^{13}C spectrum in Figure S12a (Supporting Information) possesses major signals at 172 and 52 ppm, consistent with formate (HCOO) and methoxide (OCH_3) species, respectively.^[29,30] In addition, a weaker peak at 88 ppm was observed, which we tentatively assign to an $\text{O}-\text{CH}_2-\text{O}$ intermediate formed upon transfer of hydride to formate (see next). Quantification of the three species (using NMR experiments with direct excitation) yielded a ratio of $0.5:0.2:1.0$ ($\text{HCOO}:\text{OCH}_2\text{O}:\text{OCH}_3$). Notably, $2\text{D } ^1\text{H}-^{13}\text{C}$ correlation NMR experiments indicate that all three species are near B–H species^[31] (Figure S12b, Supporting Information). Thus, the results from SSNMR corroborate the results from our other spectroscopic analyses while also revealing the potential intermediacy of a partially reduced $\text{O}-\text{CH}_2-\text{O}$ species. To better understand the reaction between MBHg and CO_2 , we

also performed X-ray absorption spectroscopy (XAS) measurements in combination with first-principle simulations. The dominant B K-edge spectroscopic signature at ≈ 194 eV is primarily attributed to trigonal coordination of B by O, which is well-reproduced by first-principles simulations of bulk B_2O_3 which comprises trigonal BO_3 units (Figure 3c). The broad, low-energy feature centered at ≈ 192 eV can be ascribed to the BH_4^- anion and is reproduced by simulated spectra for bulk γ - $Mg(BH_4)_2$. In our experimental setup, we measured both the bulk sensitive total fluorescence yield (TFY) and surface sensitive total electron yield (TEY) spectra, which show that the surface of pristine MBH (pink lines) is slightly more oxidized than the bulk (Figure 3c). Although the samples were handled in an air-free atmosphere for the XAS measurements, the data suggest that the sample was oxidized to some degree, which is corroborated by analysis of the IR spectra. In Figure 3a, the peak at ≈ 900 cm^{-1} is assigned to the boroxol rings of B_2O_3 ^[32] and the absorption band located between 1300 and 1450 cm^{-1} is attributed to the B–O bond of the oxidized species (e.g., $B(OH)_3$ or $B(OH)_4^-$).^[33,34] In addition, we performed in situ O K-edge XAS measurements in combination with first-principles simulations (Figure S13, Supporting Information). Upon CO_2 uptake, a shoulder appears below 535 eV, which we interpret as belonging to newly formed oxygen-containing species, such as $-CH=O$ and $Mg-O-B$, based on our simulations.

In order to understand the uptake mechanism uncovered by this analysis, we turned to first-principles simulations to examine the energetics of formate and methoxide formation in MBH (Figure 4a). The reaction of one molecule of CO_2 with a BH_4^- anion to form $(HCOO-BH_3)^-$ is predicted to be exothermic, releasing 0.35 eV per molecule of CO_2 . Once the $(HCOO-BH_3)^-$ intermediate is formed, H^- transfer could hypothetically occur to create $-CH_2-$ and $-CH_3$ containing species, as shown in Figure S14 (Supporting Information). Although the entire reaction from $(HCOO-BH_3)^-$ to $(CH_3O-BH_3)^-$ can release 2.18 eV per unit, the formation of intermediate $-OCH_2-O-BH_2$ is only slightly exothermic (0.11 eV). This may explain the low amount of this intermediate observed by SSNMR (Figure S12, Supporting Information). Instead, the formate-substituted borohydride $(HCOO-BH_3)^-$ unit is thermodynamically more favored to react with a second CO_2 molecule, releasing 0.85 eV. The fact that the reaction of a second molecule of CO_2 with the BH_4^- sites is thermodynamically more favorable than the reaction of the first molecule of CO_2 may explain the sudden uptake of CO_2 in volumetric experiments (Figure 2). The reaction of $(HCOO-BH_3)^-$ centers with CO_2 is likely faster than that of the parent BH_4^- centers, in accordance with the Bell–Evans–Polanyi principle. This enhanced uptake can be rationalized by considering that the estimated local atomic charge of boron (from Bader analysis) is higher (+1.78) in $(BH_3-HCOO)^-$ than in the parent BH_4^- center (+1.55), which would promote an increased interaction between an O atom of CO_2 and the B center in the former. This increased interaction should weaken the C=O bond of CO_2 and facilitate the nucleophilic transfer of hydride. After reaction of two CO_2 molecules, further reduction of formate to methoxide is more thermodynamically favorable by -2.24 eV. Notably, these calculations also suggest that the pre-oxidized form of borohydride, (BH_3-OH) , which our XAS measurements confirm

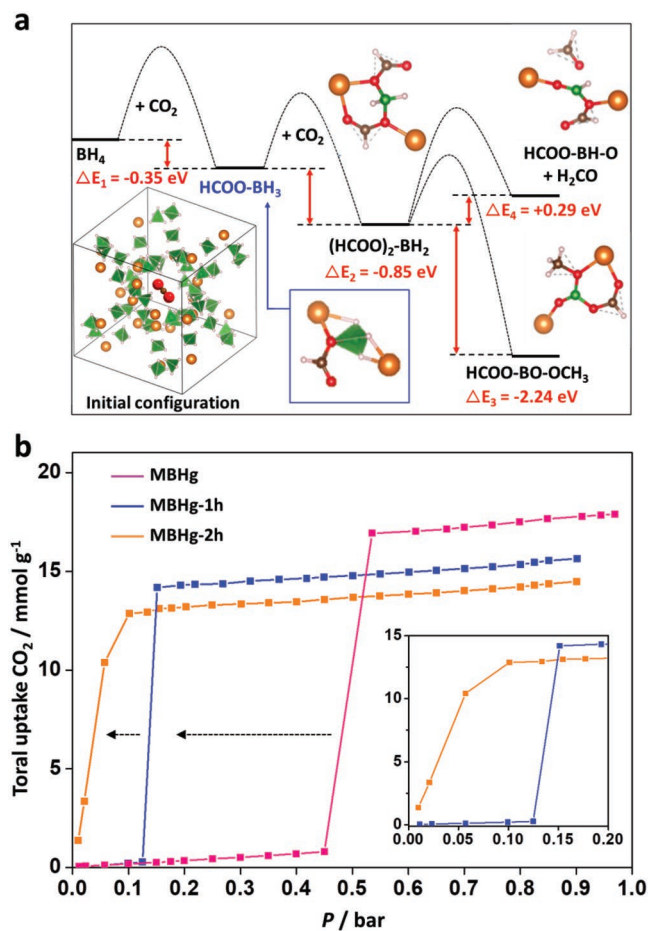


Figure 4. a) First-principle calculations of the thermodynamics of CO_2 reaction in MBH. The energies are calculated as one or two CO_2 molecules per unit cell (24 formula units) of MBH. Zero energy was chosen as the CO_2 molecule floating in the pores of MBH prior to reaction. The orange, green, red, brown, and pink spheres represent Mg, B, O, C, and H atoms, respectively. The BH_3 and BH_4^- units are shown as green polyhedra. b) 25 °C CO_2 uptake profiles of MBHg and MBHg pretreated with 0.5 bar of CO_2 for 1 or 2 h (MBHg-1h and MBHg-2h, respectively). The inset shows an expansion of the low-pressure region.

is present to some degree in the parent material, also demonstrates increasingly thermodynamically favorable reactions with CO_2 (Figure S15, Supporting Information). To summarize, these spectroscopic measurements and first-principles simulations support that pristine MBHg reacts with CO_2 first to form predominantly formate in MBHg-1h. During further reaction to form MBHg-2h, we observe a continuation of the thermodynamically favorable reduction of CO_2 to formate, as well as reduction of formate to methoxide (MBHg-2h) (Figure 3d).

Given the results from these systematic experiments and first-principles calculations, we hypothesized that the intermediate formate-functionalized materials, MBHg-1h and MBHg-2h, should be more thermodynamically and kinetically prone to react with CO_2 than pristine MBHg. To investigate this possibility, the 25 °C CO_2 uptake profiles of pristine MBHg were compared with those of MBHg-1h and MBHg-2h (Figure 4b). Consistent with our computational findings (Figure 4a) and results with longer equilibration times (Figure S7, Supporting

Information), the reaction efficiency at lower pressures dramatically increases with increasing $(\text{BH}_3\text{-HCOO})^-/\text{BH}_4^-$ ratios. For example, the 0.15 bar CO_2 uptake capacities of MBHg-1h (14.1 mmol g^{-1}) and MBHg-2h (13.1 mmol g^{-1}) are significantly higher than pristine MBHg ($0.255 \text{ mmol g}^{-1}$) under these conditions, and MBHg-2h possesses a high uptake (10.4 mmol g^{-1}) even at the lower pressure of 0.05 bar (Figure 4b, inset). Considering the kinetically controlled nature of these measurements, these results indeed suggest that MBHg-1h and MBHg-2h react more rapidly with CO_2 than pristine MBHg. Given the lower surface areas of MBHg-1h and MBHg-2h compared to MBHg, this increased rate of reaction is likely not due to an increase in the rate of diffusion in the material. Rather, these results suggest that the intermediate $(\text{BH}_3\text{-HCOO})^-$ centers present in MBHg-1h and MBHg-2h are more reactive toward CO_2 than the parent BH_4^- centers.

To test this hypothesis further, we measured the CO_2 reaction kinetics of MBHg, MBHg-1h, and MBHg-2h from a 15% CO_2 in N_2 stream via thermogravimetric analysis (Figure 5).^[35] The kinetic plots in Figure 5a follow CO_2 uptake as a function of time in pristine MBHg (full plots are included in Figure S16, Supporting Information). At all temperatures examined,

a CO_2 uptake of $\geq 12 \text{ mmol g}^{-1}$ could be reached in less than 60 min, which is significantly enhanced relative to uptake in bulk MBH ($\approx 12 \text{ mmol g}^{-1}$ in 7 d at 1 bar and 30°C).^[11] In addition, similar to the behavior observed in the uptake profiles (Figure 2a), faster reaction kinetics and greater uptake of CO_2 were observed for MBHg at higher temperatures, reflecting diffusion and/or reaction-limited reaction kinetics.

A notable feature of the kinetic profile of pristine MBHg is the significant induction period observed at lower temperatures, in which the maximum rate of reaction at 50°C occurred only after the sample had been exposed to CO_2 for ≈ 45 min (Figure S17, Supporting Information). This induction period is likely due to the slow initial reaction of CO_2 with the BH_4^- anions to form $(\text{H}_3\text{B-HCOO})^-$. After reaching a critical concentration of formate species in the MBHg material, the average rate of reaction increases, owing to the increased likelihood of CO_2 reacting with a $(\text{H}_3\text{B-HCOO})^-$ site relative to a BH_4^- site. This finding is consistent with our computational predictions and agrees well with the results in Figure 2a and Figure S6 (Supporting Information). In order to model the range of resulting CO_2 reaction kinetic profiles, we evaluated both a simple pseudo-first-order kinetics model (Equation (1))

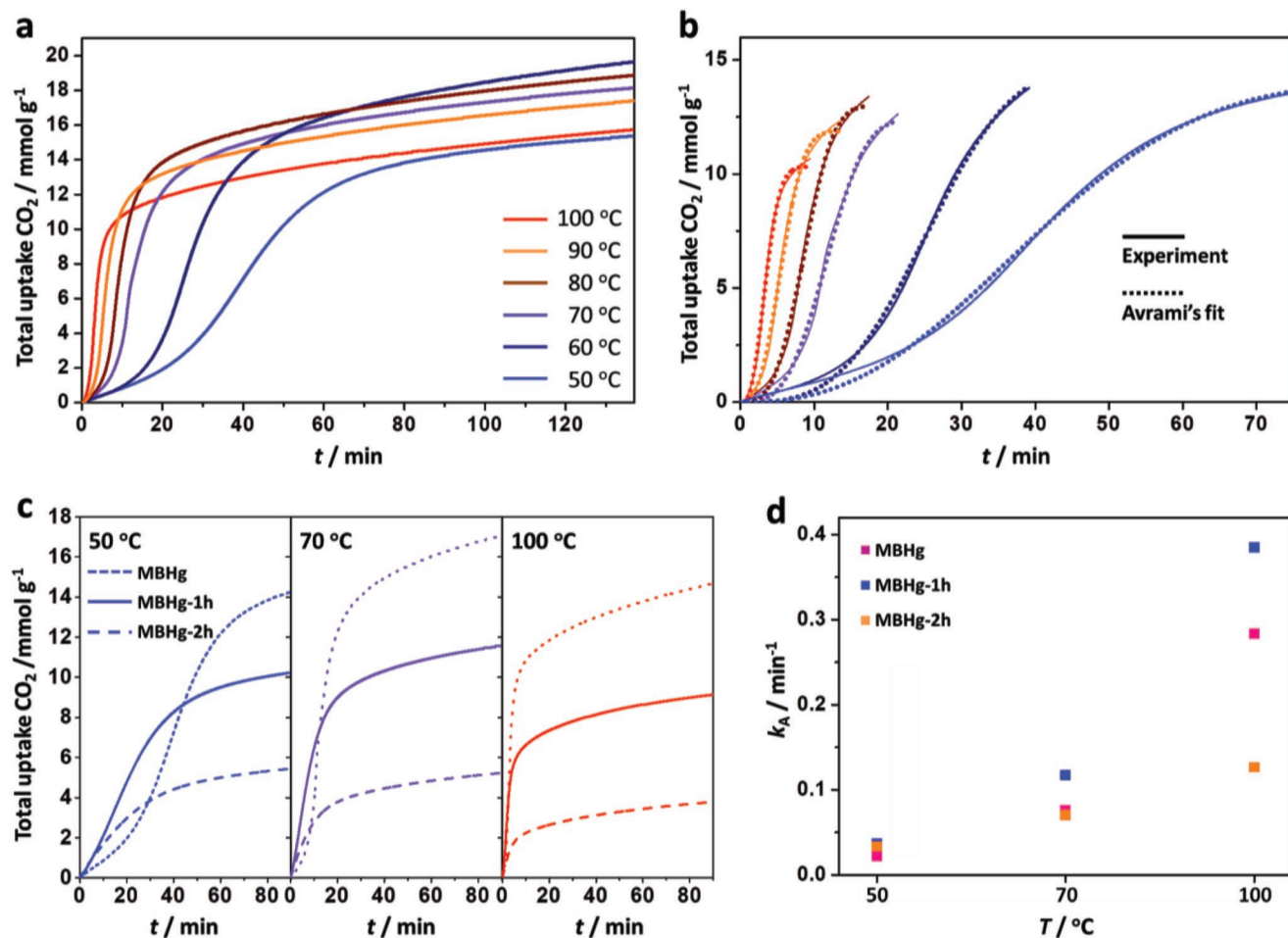


Figure 5. a) CO_2 reaction kinetics in pristine MBHg at various temperatures from a 15% CO_2 in N_2 stream. b) Avrami's fractional-order kinetic model of the experimental CO_2 uptake profiles presented in (a). c) Comparison of the gravimetric CO_2 uptake in MBHg, MBHg-1h, and MBHg-2h at three temperatures from a 15% CO_2 in N_2 stream. d) Avrami rate constant (k_A) as a function of temperature for MBHg, MBHg-1h, and MBHg-2h.

as well as Avrami's kinetics model (Equation (2)). The latter was originally developed to model nucleation-growth kinetics but has been used extensively to model kinetically dominated CO₂ chemisorption profiles resulting from complex reaction mechanisms or multiple reaction pathways.^[36–39] Therefore, the CO₂ reaction kinetics during the initial temporal phase at each temperature were modeled to calculate the uptake at time t (C_t) by fitting both the saturation uptake (C_e) as well as the first order (k_1) and Avrami (k_A) kinetic rate constants and, in the case of the Avrami model, the Avrami constant (n_A) (Figure 5b). Note that in both cases, the constant partial pressure of CO₂ is embedded in the observed rate constants

$$C_t = C_e \left[1 - e^{-(k_1 t)} \right] \quad (1)$$

$$C_t = C_e \left[1 - e^{-(k_A t)^{n_A}} \right] \quad (2)$$

In general, we found that Avrami's model provided significantly better fits to the data compared to a pseudo-first-order model (Figure S16 and Tables S3 and S4, Supporting Information). The calculated Avrami rate constants for unactivated MBHg samples varied from 0.022 at 50 °C to 0.284 at 100 °C. In addition, the Avrami exponent, n_A , was determined to be between 3 and 2 in our experiments. This finding suggests 2D growth of the reaction nuclei at the beginning of the reaction process; however, given the unconventional two-step reaction in MBHg, the same kinetics profile may be explained by other physical models for growth. For example, the initial reaction site formation on the exposed MBHg surface may be inhomogeneous.

Consistent with our mechanistic hypothesis, the induction period observed in the gravimetric uptake profile of pristine MBHg decreased in MBHg-1h and completely disappeared in MBHg-2h, likely due to the higher concentration of active (H₃B–HCOO)[–] sites in these materials compared to pristine MBHg (Figure 5c). The kinetics in MBHg-1h and MBHg-2h were also fit using Avrami's kinetic model, and at all temperatures MBHg-1h demonstrates higher rate constants, k_A , compared to pristine MBHg (Figure 5d). Reflecting the disappearance of the induction period, the average value for n_A in the Avrami fits also decreases as the sample is activated, from ≈2.6 for pristine MBHg to ≈1.5 and ≈1.0 for MBHg-1h and MBHg-2h, respectively (Figure S18, Table S4, Supporting Information). In the case of MBHg-2h, the kinetics profile could also be readily fit with a pseudo-first-order kinetics model ($n_A = 1$), reflecting the simpler reaction kinetics in this material. Overall, the experiments discussed herein are consistent with a two-step “runaway” CO₂ reaction process in these materials, in which CO₂ reaction is both more rapid and more thermodynamically favorable at metastable (H₃B–HCOO)[–] sites compared to the parent BH₄[–] sites.

In conclusion, we show that magnesium borohydrides can be tailored to exhibit high uptake capacity of CO₂ with fast uptake kinetics by reducing the size of MBH into nanoscale regime within a supporting matrix of rGO. This nanoscale MBHg exhibits a remarkable 260% increase in CO₂ uptake relative to bulk MBH. In addition, our density functional theory (DFT) calculations and thermogravimetric analysis (TGA)

kinetic measurements indicate that (H₃B–HCOO)[–] sites generated in situ display the most thermodynamically and kinetically favorable reaction with CO₂. Although CO₂ uptake in MBHg and its activated congeners is irreversible, its high uptake capacity compared to current state-of-the-art materials may make it promising for carbon capture applications involving disposable adsorbent materials.

Supporting Information

Supporting Information is available from the Wiley Online Library or from the author.

Acknowledgements

S.J., P.J.M., and L.F.W. contributed equally to this work. Work at the Molecular Foundry and the Advanced Light Source was supported through approved user projects. These national user facilities were supported by the Office of Science, Office of Basic Energy Sciences, of the U.S. Department of Energy under Contract No. DE-AC02-05CH11231. The authors thank Martin Kunz at the Advanced Light Source (ALS) for PXRD experimental support. The materials synthesis and structural characterization efforts were supported by the Department of Energy (DOE) through Hydrogen Materials Advanced Research Consortium (Hy-MARC), established as part of the Energy Materials Network by the U.S. Department of Energy, Office of Energy Efficiency and Renewable Energy, Fuel Cell Technologies Office, under Contract No. DE-AC02-05CH11231. Part of the computational work by L.F.W. was performed under the auspices of the U.S. Department of Energy by Lawrence Livermore National Laboratory under Contract No. DE-AC52-07NA27344. Gas uptake measurements were supported through the Center for Gas Separations, an Energy Frontier Research Center funded by the U.S. Department of Energy, Office of Science, Office of Basic Energy Sciences under award DE-SC0001015. The authors thank the National Institute of General Medical Science of the National Institutes of Health for a postdoctoral fellowship for P.J.M. (F32GM120799). The content is solely the responsibility of the authors and does not necessarily represent the official views of the National Institutes of Health. The authors are grateful to Dr. Katie R. Meihaus for editorial assistance. A.C.F. thanks Jeffrey Reimer for support. This work was authored in part by the National Renewable Energy Laboratory, operated by Alliance for Sustainable Energy, LLC, for the U.S. Department of Energy (DOE) under Contract No. DE-AC36-08GO28308.

Conflict of Interest

The authors declare no conflict of interest.

[1] R. S. Haszeldine, *Science* **2009**, 325, 1647.

[2] A.-H. Lu, G.-P. Hao, *Annu. Rep. Prog. Chem., Sect. A: Inorg. Chem.* **2013**, 109, 484.

- [3] K. Sumida, D. L. Rogow, J. A. Mason, T. M. McDonald, E. D. Bloch, Z. R. Herm, T.-H. Bae, J. R. Long, *Chem. Rev.* **2011**, 112, 724.
- [4] A. Armutlulu, M. A. Naeem, H. J. Liu, S. M. Kim, A. Kierzkowska, A. Fedorov, C. R. Müller, *Adv. Mater.* **2017**, 29, 1702896.
- [5] M. Nandi, K. Okada, A. Dutta, A. Bhaumik, J. Maruyama, D. Derks, H. Uyama, *Chem. Commun.* **2012**, 48, 10283.
- [6] L. Xiang, L. Sheng, C. Wang, L. Zhang, Y. Pan, Y. Li, *Adv. Mater.* **2017**, 29, 1606999.
- [7] Y. Lin, C. Kong, L. Chen, *RSC Adv.* **2016**, 6, 32598.
- [8] T. M. McDonald, J. A. Mason, X. Kong, E. D. Bloch, D. Gygi, A. Dani, V. Crocella, F. Giordanino, S. O. Odoh, W. Drisdell, B. Vlasisavljevich, A. L. Dzubak, R. Poloni, S. K. Schnell, N. Planas, K. Lee, T. Pascal, L. F. Wan, D. Prendergast, J. B. Neaton, B. Smit, J. B. Kortright, L. Gagliardi, S. Bordiga, J. A. Reimer, J. R. Long, *Nature* **2015**, 519, 303.
- [9] A. A. Olajire, *Renewable Sustainable Energy Rev.* **2018**, 92, 570.
- [10] J.-H. Lee, R. L. Siegelman, L. Maserati, T. Rangel, B. A. Helms, J. R. Long, J. B. Neaton, *Chem. Sci.* **2018**, 9, 5197.
- [11] J. A. Mason, K. Sumida, Z. R. Herm, R. Krishna, J. R. Long, *Energy Environ. Sci.* **2011**, 4, 3030.
- [12] T. M. McDonald, W. R. Lee, A. J. Mason, B. M. Wiers, C. S. Hong, J. R. Long, *J. Am. Chem. Soc.* **2012**, 134, 7056.
- [13] Wieland, P. O. NASA/TM-98-206956/VOL1; NASA Marshall Space Flight Center: Marshall Space Flight Center, AL, USA 1998; Ch. 3.3.1, p. 121.
- [14] Y. Filinchuk, B. Richter, T. R. Jensen, V. Dmitriev, D. Chernyshov, H. Hagemann, *Angew. Chem., Int. Ed.* **2011**, 50, 11162.
- [15] J. G. Vitillo, E. Groppo, E. G. Bardají, M. Baricco, S. Bordiga, *Phys. Chem. Chem. Phys.* **2014**, 16, 22482.
- [16] Y. Zhao, Z. Zhang, *Chem. Eng. Technol.* **2015**, 38, 110.
- [17] T. Wartik, R. K. Pearson, *J. Inorg. Nucl. Chem.* **1958**, 7, 404.
- [18] P. Zanella, L. Crociani, N. Masciocchi, G. Giunchi, *Inorg. Chem.* **2007**, 46, 9039.
- [19] E. S. Cho, M. Anne, S. A. Ruminski, Y.-S. Liu, J. Guo, J. J. Urban, *Nat. Commun.* **2016**, 7, 10804.
- [20] A. Roesch, E. P. Reddy, P. G. Smirniotis, *Ind. Eng. Chem. Res.* **2005**, 44, 6485.
- [21] S. Wang, S. Yan, X. Ma, J. Gong, *Energy Environ. Sci.* **2011**, 4, 3805.
- [22] H. J. Kim, S.-M. Lee, Y.-S. Oh, Y.-H. Yang, Y. S. Lim, D. H. Yoon, C. Lee, J.-Y. Kim, R. S. Ruoff, *Sci. Rep.* **2014**, 4, 5176.
- [23] O. Zavorotynska, A. El-Kharbachi, S. Deledda, B. C. Hauback, *Int. J. Hydrogen Energy* **2016**, 41, 14387.
- [24] J. Zhang, Y. Zhao, D. L. Akins, J. W. Lee, *J. Phys. Chem. C* **2011**, 115, 8386.
- [25] R. J. Newhouse, V. Stavila, S.-J. Hwang, L. E. Klebanoff, J. Z. Zhang, *J. Phys. Chem. C* **2010**, 114, 5224.
- [26] I. Knopf, C. C. Cummins, *Organometallics* **2015**, 34, 1601.
- [27] K. A. Grice, M. C. Groenenboom, J. D. A. Manuel, M. A. Sovereign, J. A. Keith, *Fuel* **2015**, 150, 139.
- [28] Y. Filinchuk, R. Cerny, H. Hagemann, *Chem. Mater.* **2009**, 21, 925.
- [29] G. Kieslich, A. C. Forse, S. Sun, K. T. Butler, S. Kumagai, Y. Wu, M. R. Warren, A. Walsh, C. P. Grey, A. K. Cheetham, *Chem. Mater.* **2016**, 28, 1312.
- [30] R. Xiong, X. Li, A. Byeon, J. W. Lee, *RSC Adv.* **2013**, 3, 25752.
- [31] R. Mohtadi, M. Matsui, T. S. Arthur, S.-J. Hwang, *Angew. Chem., Int. Ed.* **2012**, 51, 9780.
- [32] E. Culea, I. Bratu, *Acta Mater.* **2001**, 49, 123.
- [33] D. Peak, G. W. Luther III, D. L. Sparks, *Geochim. Cosmochim. Acta* **2003**, 67, 2551.
- [34] W. Zhang, T. Liu, J. Xu, *SpringerPlus* **2016**, 5, 1202.
- [35] E. R. Monazam, L. J. Shadle, D. C. Miller, H. W. Pennline, D. J. Fauth, J. S. Hoffman, M. L. Gray, *AIChE J.* **2013**, 59, 923.
- [36] M. Avrami, *J. Chem. Phys.* **1941**, 9, 177.
- [37] Q. Liu, J. Shi, S. Zheng, M. Tao, Y. He, Y. Shi, *Ind. Eng. Chem. Res.* **2014**, 53, 11677.
- [38] Y.-S. Liu, P.-A. Glans, C.-H. Chuang, M. Kapilashrami, J. Guo, *J. Electron Spectrosc. Relat. Phenom.* **2015**, 200, 282.
- [39] R. Serna-Guerrero, A. Sayari, *Chem. Eng. J.* **2010**, 161, 182.